Systematics of nuclear charge distributions in Fe, Co, Ni, Cu, and Zn deduced from muonic x-ray measurements*

E. B. Shera, E. T. Ritter,† R. B. Perkins, G. A. Rinker, and L. K. Wagner‡
University of California, Los Alamos Scientific Laboratory, Los Alamos, New Mexico 87545

H. D. Wohlfahrt and G. Fricke
University of Mainz, Mainz, Germany

R. M. Steffen
Purdue University, Lafayette, Indiana 47907

(Received 12 April 1976)

The results of precise measurements of the energies of the $2p_{3/2} \rightarrow 1s_{1/2}$ and $2p_{1/2} \rightarrow 1s_{1/2}$ muonic x-ray transitions of ^{54}Fe, ^{56}Fe, ^{57}Fe, ^{58}Fe, ^{59}Co, ^{58}Ni, ^{60}Ni, ^{61}Ni, ^{62}Ni, ^{64}Ni, ^{63}Cu, ^{65}Cu, ^{64}Zn, ^{66}Zn, ^{68}Zn, and ^{70}Zn are reported. Using a highly linear digitally stabilized Ge(Li) spectrometer system, the absolute energies and energy shifts between nuclei were measured with total errors of approximately 40–60 eV (110 eV for ^{70}Zn). The data were analyzed in terms of the Barrett moments $\langle r^k e^{-ar} \rangle$ of the nuclear charge distributions from which the equivalent nuclear radii R_k and the isotopic and isotonic differences δR_k were computed. Particular attention was given to higher-order corrections of the energies of the muonic states. Appropriate quantum-electrodynamical corrections were calculated to all significant orders. Nuclear polarization corrections for multipole interactions up to and including $L = 4$ were computed for each isotope. The $\Delta A = 2$ isotone shifts δR_k for even A isotopes show a strong shell closure effect at $Z = 28$, which is quite independent of the neutron number. The $\Delta N = 2$ isotope shifts between even nuclei decrease smoothly and uniformly with increasing N from $N = 28$ to $N = 40$ and are essentially independent of Z. This unexpected behavior suggests that the added neutrons interact with the entire proton core rather than with the valence protons. The $\Delta N = 1$ isotope shift results show a pronounced odd-even staggering effect, which, however, is somewhat smaller than theoretical predictions. The isotone series ^{58}Fe-^{59}Co-^{60}Ni, which is just below the $Z = 28$ shell closure, shows strong odd-even staggering, whereas the series ^{64}Ni-^{65}Cu-^{66}Zn and ^{62}Ni-^{63}Cu-^{64}Zn just above $Z = 28$ exhibit only a very small staggering effect. A comparison of the experimental data of the rms radii $\langle r^2 \rangle^{1/2}$ with the results of spherically constrained Hartree-Fock calculations shows good agreement for all four Zn isotopes and the heavier Ni isotopes (^{60}Ni, ^{62}Ni, ^{64}Ni), but poor agreement for the Fe isotopes and ^{58}Ni.

[NUCLEAR STRUCTURE, MOMENTS ^{54,56,57,58}Fe, ^{59}Co, ^{58,60,61,62,64}Ni ^{63,65}Cu, ^{64,66,68,70}Zn; measured muonic x-ray spectra; deduced nuclear charge parameters, isotope and isotone shifts. Calculated quantum-electrodynamic and nuclear-polarization corrections. Compared charge parameters with Hartree-Fock calculations.]

I. INTRODUCTION

Detailed investigation of the rearrangement of the nuclear charge distribution in response to the addition of neutrons or protons throughout a whole series of isotopes provides a valuable and stringent test of one's understanding of the structure of nuclear ground states.

The usual expression for nuclear radii, $R = r_0 A^{1/3}$, which can be derived on the basis of a classical liquid drop model, represents only a crude average as A varies along the stability valley in an N versus Z plot. The average $A^{1/3}$ behavior does, however, serve as a useful standard of comparison from which to judge individual variations of the charge radius. Figure 1 presents the existing muonic isotope shift data[1] for even nuclei in the region $A = 20$–126. To emphasize the departure from $A^{1/3}$ behavior the experimental shift values have been divided by the "standard" shift $\delta R_k^{\text{std}} = 1/3(\Delta A/A)R_k$ (the Barrett equivalent radius R_k is defined in Sec. II). The figure illustrates that the $A^{1/3}$ behavior is strongly modified by nuclear shell structure. One observes that the isotope shifts are largest at the beginning of a neutron shell and become quite small (in fact, negative in two regions) just before the major shell closures at $N = 28$, 50, 82, and 126.

In the present paper, results for muonic atoms from the lightest stable Fe ($A = 54$) to the heaviest stable Zn ($A = 70$) are reported.[2] In this range of nuclei one observes the effect of adding nucleons in the $2p_{3/2}$, $1f_{5/2}$, and $2p_{1/2}$ neutron shells and the $1f_{7/2}$ and $2p_{3/2}$ proton shells.

It was the goal of this experiment to determine accurate differences of nuclear charge distribu-

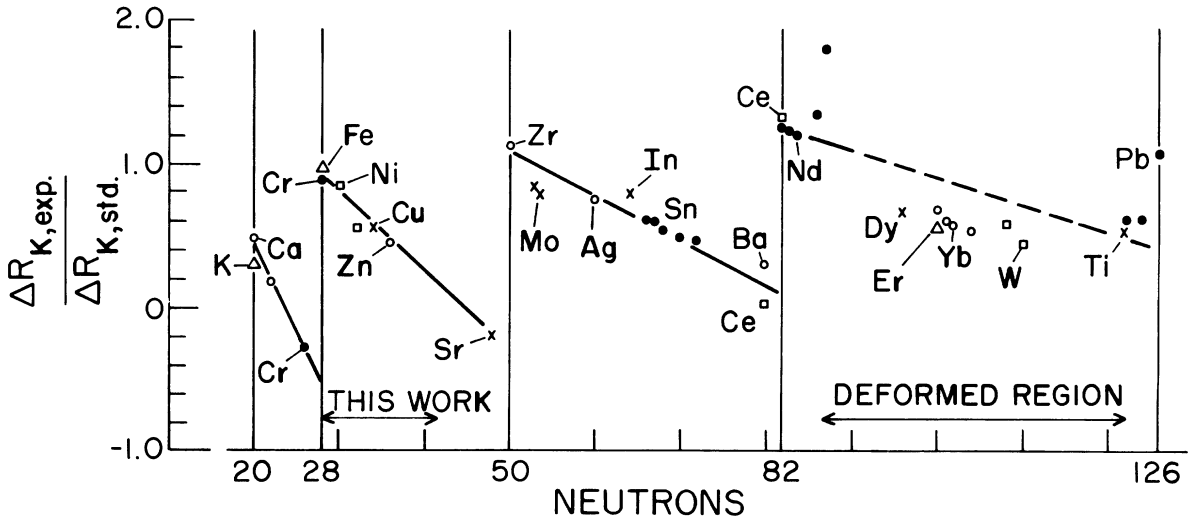

FIG. 1. Summary of existing isotope shift data for $\Delta N = 2$. ΔR_k is the change in the Barrett equivalent radius measured by the $2p_{3/2}$-$1s_{1/2}$ muonic x-ray transition. The data are from the compilations of Engfer *et al.* (Ref. 1). The $^{138-140}$Ce and $^{210-212}$Pb data are optical isotope shift results from K. Heilig and A. Stendel, At. Data Nucl. Data Tables 14, 613 (1974).

tion parameters in the vicinity of the magic proton number 28 and to find if the systematic features which are apparent in Fig. 1 also occur when a sequence of nuclei is studied in detail.

II. NUCLEAR CHARGE DISTRIBUTION PARAMETERS AND MUONIC ISOTOPE AND ISOTONE SHIFTS

The muon binding energies of isotopes of the same element differ slightly from each other, and these differences give rise to small displacements in the muonic x-ray spectra. These so-called isotope shifts are caused mainly by two effects: the "mass shift," which is a result of the difference in reduced mass of systems with different nuclear masses, and the "field shift" which is caused by differences in the size of the charge distribution for different isotopes.

The "field shift" has been used in this work to determine differences in the effective radii of charge distributions of various nuclei. In first-order perturbation theory the energy shift of a muonic transition between the levels i and f due to a change of the spherical charge distribution $\Delta\rho(r)$ is given by

$$\Delta E = Z \int \Delta\rho(r)[V_\mu^i(r) - V_\mu^f(r)]4\pi r^2 dr, \qquad (1)$$

where $V_\mu(r)$ is the potential generated by the bound muon in a particular state.

The observed muonic transition energies can be used to determine the parameters of an assumed charge distribution $\rho(r)$. This is done using an iterative procedure which involves solving the Dirac equation for an approximate set of charge parameters and then adjusting these parameters to bring the calculated transition energies into agreement with the observed values. Appropriate higher-order corrections to the calculated energies must also be included (see Sec. III). The potential $V_\mu(r)$ can then be calculated from the components $f_\mu(r)$ and $g_\mu(r)$ of this solution of the Dirac equation. Calculations performed with various assumed charge distributions have shown that the resulting $V_\mu(r)$ is quite insensitive to the initial choice of $\rho(r)$.

It has been shown by Ford and Wills[3] that the potential difference $V_\mu^i(r) - V_\mu^f(r)$ in the region of overlap between the nuclear charge distribution and the muon wave function can be approximated to a high degree of accuracy by a simple analytic form. The best form currently available is due to Barrett[4]:

$$V_\mu^i(r) - V_\mu^f(r) = A + Br^k e^{-\alpha r}. \qquad (2)$$

The value of k in this equation is different for different transitions and also varies slowly as a function of Z for a given transition. The value of α varies linearly[1] with Z and is usually kept fixed for all transitions of one element.

From the fitted potential [Eq. (2)] a generalized moment of the nuclear charge distribution can be defined as

$$\langle r^k e^{-\alpha r}\rangle = \int \rho(r) r^k e^{-\alpha r} 4\pi r^2 dr, \qquad (3)$$

and an equivalent nuclear charge radius R_k can be computed which corresponds to the radius of

a sphere of constant charge density that gives the same value of $\langle r^k e^{-\alpha r}\rangle$. Thus, R_k is defined by the equation:

$$3R_k^{-3}\int_0^{R_k} r^k e^{-\alpha r} r^2 dr = \langle r^k e^{-\alpha r}\rangle. \quad (4)$$

Since the values of k and α are quite insensitive to the initial choice of $\rho(r)$ and the analytical expression chosen in Eq. (2) fits the potential difference to a high degree of accuracy, R_k is a nearly model-independent way of characterizing the nuclear charge distribution as probed by a particular muonic transition.

For all the isotopes of a single element the parameters α and k are essentially identical for a given transition, and the "field shift" is given by a relation with the same form as Eq. (1), namely:

$$\Delta E_{\mathrm{FS}} = ZB\int \Delta\rho r^k e^{-\alpha r} 4\pi r^2 dr. \quad (5)$$

The differences of the equivalent radii δR_k can be calculated by Eqs. (3) and (4).

The muonic x-ray spectra of *isotones* differ considerably from each other because, in addition to the mass and field effects mentioned above, the nuclei have different charges. Thus, different values of α and k are appropriate for each nucleus. Also, the strong Z dependence of muonic transition energies makes the perturbation approach, which is satisfactory for isotopes, less useful for isotones. It is more straightforward to extract Barrett radii by direct numerical fits of the charge distribution parameters to the experimental energies. The differences of the equivalent radii δR_k obtained in this way are essentially model independent; however, it should be kept in mind that slightly different moments of the charge distribution are compared in the case of isotones.

The finite extension of the nuclear charge distribution has the most pronounced effect on the binding energy of the $1s$ state. In fact, in the $A = 60$ mass region, only the $1s$ state shows a finite size effect which is large compared with the achievable experimental accuracy. For this reason the present work was concentrated on accurate measurements of the $2p_{3/2}$-$1s_{1/2}$ and $2p_{1/2}$-$1s_{1/2}$ muonic transitions.

III. HIGHER-ORDER CORRECTIONS

All known important higher-order energy corrections of the muonic levels were taken into account in the analysis. The computed magnitudes of these corrections for selected isotopes are summarized in Table I. The largest correction is the e^+e^- vacuum polarization of order $\alpha Z\alpha$ depicted diagrammatically in Fig. 2(a). The total correction, including "ladder" iterations of the basic diagram, is obtained by inserting the "Uehling" potential[5] into the Dirac equation before it is solved.[6] The closely related e^+e^- vacuum polarization of order $\alpha^2 Z\alpha$ [Fig. 2(b), the Källen-Sabry term][7] was included in a similar way.[6,8] The additional electron vacuum polarization effects of order $\alpha(Z\alpha)^{n\geq 3}$ arising from the diagrams in Fig. 2(c) have been taken from the literature.[9] The only other e^+e^- vacuum polarization diagrams of low order are those of Fig. 2(d), which were not included in the fitting procedure as they are known to be negligibly small.[10] Additional electronic effects arise from the screening of the nuclear charge by the atomic electrons. These effects were computed[11] using true Hartree-Fock electron densities of the neutral atom with charge $Z - 1$ (the "$Z - 1$" approximation).

Additional quantum-electrodynamic effects arise from the vertex correction of order $\alpha Z\alpha$ [Fig. 2(e)], which contributes most of the anomalous magnetic moment as well as a central field interaction. These effects were computed by standard means,[12] using the Bethe-Negele bounds on the "Bethe sum."[13] The vertex correction of order $\alpha(Z\alpha)^2$ [Fig. 2(f)] has been estimated[12] but not accurately computed. One-half of this estimate has been included here as a correction of the energy, with an uncertainty equal to the included contribution. In addition, $\mu^+\mu^-$ vacuum polarization[12] [Fig. 2(g)] and (relativistic) nuclear recoil[14] corrections were computed using prescriptions given in the literature.

All of these higher-order corrections can be computed with an uncertainty of a few eV or less with the exception of the vertex corrections. The $\alpha(Z\alpha)$ correction has a large uncertainty which is mainly caused by the difficulties in calculating the so-called Bethe sum. The bounds given in Ref. 13 produce strict error limits for the muon $1s$ state, where the correction is large, but not for the $2p$ states, where the correction is small. The $\alpha(Z\alpha)^2$ correction is relatively more uncertain but smaller. Magnitudes of these error estimates are noted in Table I. A separate but related question concerns the numerical accuracy with which these corrections, as well as the unperturbed binding energies, are computed. Calculations which appear in the literature disagree with one another by as much as several tens of eV; presumably, this is due to limited numerical accuracy. For the calculations reported here, we have made an exhaustive investigation of the numerical accuracy and are confident that numerical errors are less than 1 eV.

The final correction to be considered is that caused by the polarization of the nuclear charge

TABLE I. Corrections to muon binding energies (keV) for selected isotopes and estimated uncertainties in these quantities. Fundamental constants used were $\alpha = 1/137.03604$, $\hbar c = 197.328\,57$, $m_\mu = 105.659\,48$, $m_e = 0.511\,0034$, amu = 931.504. Estimated errors due to uncertainties in these constants are combined quadratically with the other theoretical error estimates.

Isotope		^{56}Fe			^{62}Ni			^{66}Zn	
Nuclear mass (amu)		55.935			61.928			65.926	
Fermi function parameters:									
c (fm)		4.04735			4.20767			4.36910	
a (fm)		0.55			0.55			0.55	
State	$1s_{1/2}$	$2p_{1/2}$	$2p_{3/2}$	$1s_{1/2}$	$2p_{1/2}$	$2p_{3/2}$	$1s_{1/2}$	$2p_{1/2}$	$2p_{3/2}$
Uncorrected energy	1722.133	479.468	475.379	1966.632	556.988	551.548	2220.605	640.418	633.337
Nuclear polarization:									
$l=0$	0.327	0.001	0	0.431	0.001	0.001	0.540	0.002	0.001
$l=1$	0.113	0.003	0.003	0.145	0.006	0.006	0.168	0.007	0.007
$l=2$ [a]	0.102	0.004	0.004	0.080	0.003	0.003	0.150	0.010	0.009
$l=2$ [b]	0.033	0	0	0.040	0.001	0.001	0.047	0.001	0.001
$l=3$	0.011	0	0	0.014	0	0	0.017	0	0
$l=4$	0.003	0	0	0.004	0	0	0.005	0	0
Vacuum polarization:									
$\alpha(Z\alpha)$	11.850	1.877	1.820	13.632	2.295	2.214	15.461	2.761	2.655
$\alpha^2(Z\alpha)$	0.095	0.013	0.012	0.109	0.016	0.016	0.124	0.020	0.019
$\alpha(Z\alpha)n \geq 3$	−0.012	−0.003	−0.003	−0.015	−0.004	−0.004	−0.019	−0.006	−0.006
Muon $\alpha(Z\alpha)$	0.029	0	0	0.035	0	0	0.042	0	0
Electron screening	0	0.001	0.001	0	0.001	0.001	0	0.001	0.001
Vertex corrections									
$\alpha(Z\alpha)$	−0.451	0.003	−0.005	−0.538	0.003	−0.008	−0.629	0.003	−0.011
$\alpha(Z\alpha)^2$	−0.024	−0.001	−0.001	−0.028	−0.001	−0.001	−0.032	−0.001	−0.001
Nuclear recoil	0.058	0.003	0.003	0.068	0.003	0.003	0.081	0.004	0.004
Total	1734.267	481.369	477.213	1980.609	559.312	553.780	2236.560	643.220	636.016
Estimated uncertainties:									
Nuclear polarization	0.236	0.003	0.003	0.285	0.004	0.004	0.371	0.008	0.007
$\alpha(Z\alpha)$ vertex	0.076	0.001	0.001	0.087	0.001	0.001	0.096	0.001	0.001
$\alpha(Z\alpha)^2$ vertex	0.024	0.001	0.001	0.028	0.001	0.001	0.032	0.001	0.001
Constants	0.006	0.002	0.002	0.007	0.002	0.002	0.008	0.002	0.002
Quadratic total	0.250	0.004	0.004	0.300	0.005	0.005	0.380	0.008	0.007

[a] From low-lying states.

[b] From the assumed quadrupole resonance.

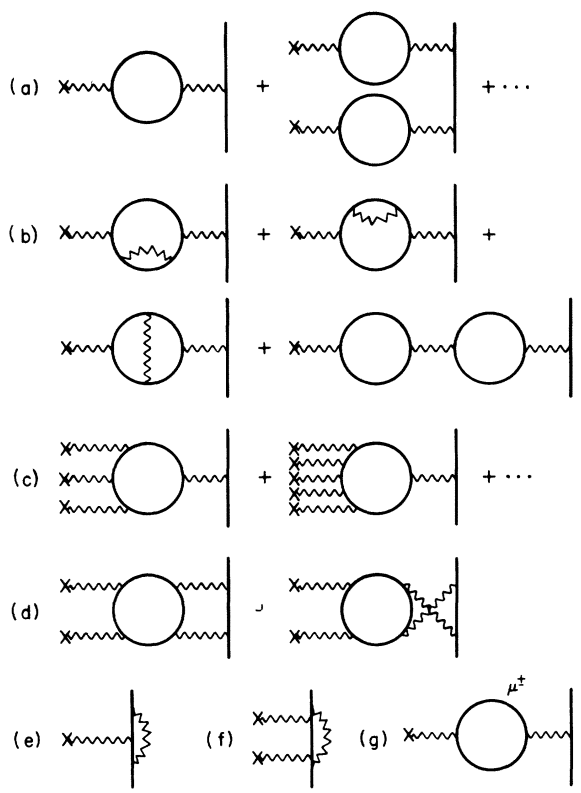

FIG. 2. (a)–(g) Quantum electrodynamic corrections to muonic-atom energy levels. Vertical lines represent the (bound) muon, × represents a static nuclear vertex, and loops represent electrons except for (g), where the loop represents muons.

distribution in the presence of the muon, i.e., the second order (two-photon exchange) perturbation correction to the energy, where the intermediate states include all possible virtual excitations of the muon and the nucleus. Detailed nuclear polarization calculations have not previously been made for the nuclei considered here. The computation of this correction ΔB_{NP} is complicated by the fact that the properties (energy, angular momentum, transition matrix elements) of only a few low-lying excited states of these nuclei are known. The influence of the great majority of the excited states can only be estimated by using photonuclear reaction or charged-particle scattering data, if they are available with sufficient accuracy, or by using sum-rule considerations or specific theoretical nuclear models. The present calculation is based primarily on sum rules, due to the lack of experimental information and absence of good theoretical models of these nuclei. In the present analysis, nuclear polarization corrections $\Delta B_{NP}(L)$ have been computed for electric monopole ($L=0$), dipole ($L=1$), quadrupole ($L=2$), octupole ($L=3$), and hexadecapole ($L=4$) excitations. In the low-lying spectra, only the experimental strengths of $E2$ excitations are consistently available for the nuclei under consideration. Nuclear polarization energy shifts for these known $E2$ excitations have been computed explicitly, using a relativistic Green's function technique described elsewhere.[15] The remaining nuclear excitations are accounted for by means of sum rules.

The isovector dipole sums have been the most thoroughly investigated. The Thomas-Reiche-Kuhn (TRK) (σ_0) and Migdal (σ_{-2}) photoabsorption sum rules are well satisfied experimentally for ^{59}Co, although not for the other nuclei in this region.[16] These other nuclei exhibit considerably less strength, presumably because of incomplete measurements. In the absence of evidence to the contrary, we assume that all of the nuclei presently considered obey both of these sum rules, which are

$$\sigma_0 = \int_0^\infty dE\, \sigma(E) = 6\frac{NZ}{A}\,\mathrm{MeV\,fm^2}$$

and

$$\sigma_{-2} = \int_0^\infty dE\, \frac{\sigma(E)}{E^2} = 2.25\times 10^{-4} A^{5/3}\,\mathrm{fm^2\,MeV^{-1}}.$$

We concentrate the dipole strength in a single state with energy $E=(\sigma_0/\sigma_{-2})^{1/2}$ so that both sums are satisfied. This choice is motivated by the fact that the polarization energy shift is proportional to a weighted integral over the cross section; the weight varies as E^{-2} as $E\to\infty$, and somewhat less rapidly for smaller E. The (isoscalar) monopole strength from the ground state 0 to final states f is given by the sum rule[16]

$$\sum_f E_f |\langle f|r^2|0\rangle|^2 = \frac{(\hbar c)^2}{Mc^2} Z\langle 0|r^2|0\rangle \approx 41 Z A^{2/3}\,\mathrm{MeV\,fm^4},$$

where we have set $N=Z=\frac{1}{2}A$ and $\langle 0|r^2|0\rangle = A^{2/3}$. The relationship of the above matrix element to the nuclear polarization energy shift is strongly dependent upon the form assumed for the transition charge density $\langle 0|\rho(r)|f\rangle$. We choose the vibrational model result

$$\langle 0|\rho(r)|f\rangle \propto \frac{1}{r^2}\frac{d}{dr}\left(r^4\frac{d\rho_0(r)}{dr}\right),$$

where $\rho_0(r)$ is the ground-state charge distribution. We assume as before that the strength is concentrated in a single state at the energy chosen for the dipole resonance. Similarly, the isoscalar sums for $L\geq 2$ are each formed[17] by

$$\sum_f E_f B(EL;0\to f)$$

$$=\frac{L(2L+1)^2}{4\pi}\frac{Z^2(\hbar c)^2}{2AMc^2}\langle 0|r^{2L-2}|0\rangle$$

$$\approx 1.65\,L(2L+1)^2Z^2A^{(2L-5)/3}\ \text{MeV fm}^{2L}$$

and are concentrated in states at the same energy as above. In the case $L=2$, the strength accounted for in the low-lying states is subtracted from the sum.

The above considerations are intended primarily to provide evidence concerning the variation of nuclear polarization among the nuclei considered here. For the most part, the absolute values of these results should be underestimates since several modes of excitation have been ignored. Where comparison is possible, the prescriptions used here provide approximate agreement with other nuclear polarization calculations which have been made for other nuclei. The most striking disagreement is for the monopole polarization; when the present prescription is applied to the 1*s* state in ^{208}Pb, the result is ~8 keV rather than 2 to 4 keV obtained elsewhere.[18] Although there is no theoretical reason to prefer our calculation for ^{208}Pb to the others, it is well known[19] that experimental muonic atom data for ^{208}Pb favor the larger value of the nuclear polarization.

The isotopic and isotonic variations in the nuclear polarization are provided mainly by the low-lying $E2$ excitations, which typically account for ~50–80% of the $E2$ energy shift of the 1*s* state. Other variations are due to the Z and A dependence of the resonance parameters.

Values of the nuclear polarization correction as computed with the above method are listed in Tables I and VII. To obtain an estimate of the magnitude of possible errors in the absolute values of the computed nuclear polarization energy shifts, we note (see above) that other calculations[18] are 30 to 40% lower than our total (9.8 keV) for ^{208}Pb. Thus we assign an error estimate of ±40% for the absolute values, which amounts to 0.2 keV for ^{54}Fe and 0.4 keV for ^{70}Zn. Errors in the isotope shifts are probably less than 0.03 to 0.05 keV in most cases, although for nuclei in which no significant low-lying $E2$ strength is observed, the results may be incorrect if significant $E2$ excitations actually exist.

We have calculated the energy shifts of the muonic levels caused by the mixing of these levels with excited nuclear states through the dynamic electric quadrupole interaction. These shifts are negligible (<1 eV for the 2*p* states) for all the even-A nuclei considered in this paper. Some of the odd-A nuclei have low-lying excited states (14.4 and 136.5 keV in ^{57}Fe, 67.4 and 282.9 keV in ^{61}Ni) with reasonably large $B(E2)$ values. However, even in these nuclei the admixture of nuclear states is very small (<1%) and the energy shifts of the 2*p* states are less than 10 eV.

IV. EXPERIMENTAL APPARATUS

The experiment was performed at the stopped-muon channel of the Clinton P. Anderson Meson Physics Facility at Los Alamos (LAMPF) during an initial period of low-intensity accelerator operation. At the time of the experiment, the time-averaged 800-MeV proton beam current was ~7 μA; the duty factor of the accelerator is 6%. Pions, produced in a 5-cm carbon target, were collected and transported by a series of quadrupole magnets. Momentum selection was imposed upon the collected pions by two bending magnets and the pion beam then passed into an extended alternating-gradient quadrupole section in which the majority of the pions decay. The resulting muons were momentum selected by the "spectrometer" portion of the channel and focused onto the target by a final series of quadrupole magnets. The spectrometer portion of the channel was tuned to accept the backward decaying muons (momentum ≃ 120 MeV/c) from 220 MeV/c pions.

The physical arrangement of the targets is shown in Fig. 3. Signals from a conventional counter telescope, consisting of plastic scintillation counters S_1, S_2, S_3^i, and S_4 were used to identify events in which muons came to rest in one of the three targets T^i. The thickness of the polyethylene moderator M was adjusted to maximize the stopping rate in the targets. The stopping rate in a 2.5 × 7.5-cm Ni target weighing 50 g was typically 2000 sec^{-1} per μA of proton current when the muon channel was tuned to illuminate an 8 × 10-cm area.

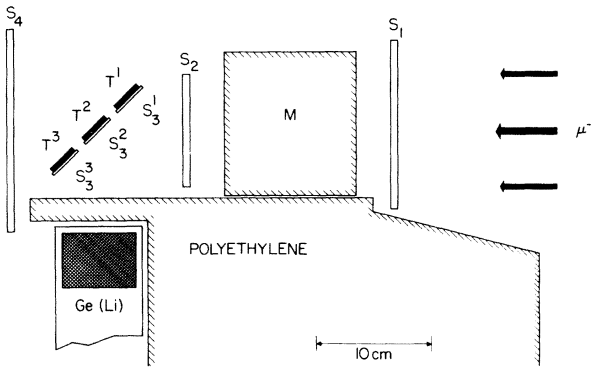

FIG. 3. Arrangement of scintillation counter telescope (S_i), muon moderator (M), targets (T^i), and Ge(Li) detector.

Muonic x rays were detected by a true-coaxial 60-cm^3 Ge(Li) detector placed at a distance of 10 cm from the center target (see Fig. 3). The Ge(Li) detector was shielded by polyethylene from scattered muons and from muons in the "halo" around the main muon beam. No high-Z shielding was used near the detector. The only significant background radiation observed with the Ge(Li) detector was due to energetic electrons from muons which decayed in the low-Z moderator. Various γ-ray sources (Table II) were located on the axis of the Ge(Li) detector at distances of 50–100 cm. These sources were always present during data runs and the associated calibration spectra were stored (in a separate section of the computer memory) simultaneously with x-ray data. To eliminate calibration errors due to any possible counting-rate dependence of electronic gain, a calibration-gating technique[20] was used which employed an auxiliary plastic scintillation counter to sample the instantaneous intensity of the muon beam. Calibration γ rays were stored only if they occurred in (accidental) coincidence with a short (~10 μs) gating signal generated by this counter. The counter was located near a bending magnet but off the axis of the muon channel so that particles which passed through it could not reach the x-ray targets. This technique insured that the calibration spectra were stored at an average rate which was proportional to the intensity of the muonic x rays. Thus any possible time-varying or count-rate-varying gain shifts should affect both x-ray and calibration spectra identically. Long-term changes in the characteristics of the linear signal path were eliminated by using digital stabilizers which were locked onto the signal from a high-stability pulser.[21]

Signals from the Ge(Li) detector were divided into one of three categories for storage depending upon their time relation t to muons stopping in the targets. If the Ge(Li) signal was in prompt coincidence ($-5\,\text{ns} < t < 5$ ns) with a stopping muon, the signal was considered a muonic x ray and was stored by the computer in a separate data array according to the target (identified by S_3^t) in which the muon stopped. Thus, the x-ray spectrum from each target was stored separately. If the Ge(Li) signal followed a muon stop ($20\,\text{ns} < t < 50$ ns), it was considered a delayed event (e.g., a nuclear γ ray) and was also stored separately according to target identification. The delayed spectra were examined for lines which could perturb the observed x-ray centroids; none were found. If the Ge(Li) signal was not related in time to a muon stop ($t > 500$ ns), it was considered a calibration γ ray and was stored accordingly, provided the calibration-gating condition mentioned above was satisfied. Ambiguous events, which, for example, might have involved near-simultaneous muon stops in two or more targets, were discarded.

The logic decisions needed to carry out these storage assignments were performed in real time

TABLE II. Energy calibration sources.

Isotope	γ-ray energy[a] (keV)
^{60}Co	1173.208 ± 0.025
	1332.464 ± 0.028
^{110m}Ag	937.483 ± 0.020
	1384.267 ± 0.029
	1475.757 ± 0.034
	1505.006 ± 0.032
	1562.264 ± 0.033
^{124}Sb	968.188 ± 0.022
	1045.106 ± 0.022
	1325.478 ± 0.029
	1368.130 ± 0.029
	1690.942 ± 0.036

[a] Energy values are from an adjustment of R. C. Greenwood and R. G. Helmer, Aerojet Nuclear Co., private communication.

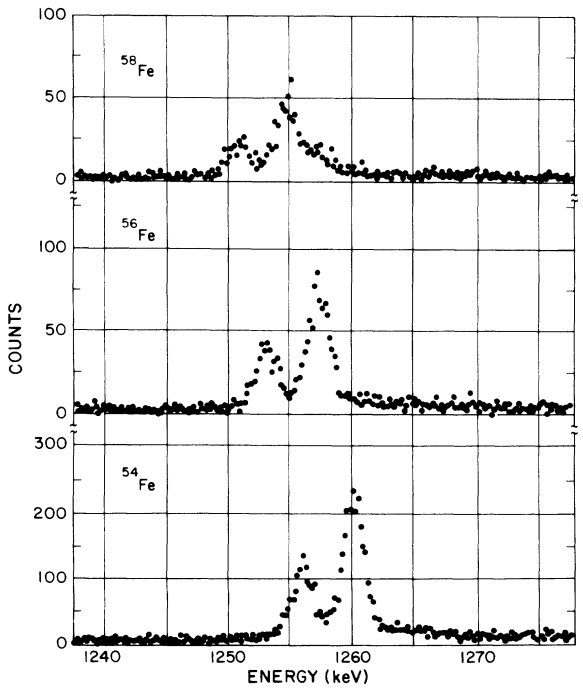

FIG. 4. Typical spectra showing the muonic $2p$–$1s$ x-ray doublet for three isotopes of Fe. The isotope shift of the x-ray energies is readily apparent. The substantial (24%) ^{56}Fe isotopic contamination of the ^{58}Fe target is also visible.

by a high-speed Camac interfaced programmable processor (MBD).[22] The digitized data were transferred by the MBD directly into serial buffer arrays in the core memory of a PDP-11 computer. When the 1000-word buffers were filled, the processor of the PDP-11 transferred the data to histograms which were stored on a fixed-head disk.

The experimenter was able to monitor the histogrammed data while it was being collected via a set of interactive display and analysis codes which ran in a background mode in the processor of the PDP-11. At the completion of a run the data arrays were transferred, using magnetic tape, to a photostorage device from which they can be accessed by a large computer for detailed analysis. Muonic x-ray spectra from three isotopes of Fe obtained during a typical run are shown in Fig. 4.

V. DATA ANALYSIS

Since the emphasis in this study was on measuring isotope and isotone shifts (i.e., *differences* in x-ray energies for neighboring nuclei), the experimental apparatus was designed so that three targets could be studied simultaneously. A total of 16 different nuclei have been studied, in various combinations of three, in such a way as to reduce the effect of systematic errors as much as possible. Table III lists the targets, their approximate masses, and their isotopic purities.

As mentioned earlier, in medium-mass nuclei only the $1s$ muonic state is significantly perturbed by the finite nuclear size and therefore only the energies of the $2p_{3/2}$-$1s_{1/2}$ ($K\alpha_1$) and $2p_{1/2}$-$1s_{1/2}$ ($K\alpha_2$) transitions were of interest in the present measurements. To understand the techniques used to analyze the spectral data it is helpful to have in mind the magnitudes of some of the physical quantities involved.

First, the resolution [full width at half maximum (FWHM)] of the detector is approximately 1.8 keV at the energies of the (Fe) $K\alpha$ lines. The fine-structure splitting of the $2p$ state (4.15 keV in Fe) is therefore almost completely resolved in the present measurements in contrast to previous measurements in this mass region (cf. Ref. 23). Thus it is possible to determine the energies of the $K\alpha_1$ and $K\alpha_2$ lines independently.

Second, isotope shifts in this mass region are approximately 1.5 keV per added neutron. Thus the measured line centroids are somewhat perturbed by the unresolved contributions of isotopic impurities in the target. This was corrected by fitting the spectral data with a multiplet of lines with intensity ratios fixed according to the isotopic composition of the target. The centroid of the principal isotopic component of the sample can thus be determined when the approximate centroids of the impurities are known. A typical value of such a correction (compared to fitting a single line) was 75 eV for the rather impure ^{57}Fe target.

Third, the muonic levels of the odd-A isotopes exhibit hyperfine (hf) structure due to interaction of the muon with nuclear magnetic and electric moments. Typically, hf splitting separates both members of the $K\alpha_1$, $K\alpha_2$ doublet into a complex pattern of lines with a maximum energy separation

TABLE III. Target masses and isotopic compositions. [Obtained on loan from the USERDA Research Materials Collection (except ^{59}Co).]

Isotope	Target mass (g)	Isotopic composition (%)
^{54}Fe	48	54—97.69, 56—2.25, 57—0.05, 58—0.01
^{56}Fe	60	54—0.03, 56—99.93, 57—0.03
^{57}Fe	48	54—0.17, 56—8.06, 57—91.66, 58—0.11
^{58}Fe	14	54—1.14, 56—23.74, 57—1.86, 58—73.26
^{59}Co	60	59—100
^{58}Ni	59	58—99.89, 60—0.11
^{60}Ni	62	58—0.21, 60—99.79
^{61}Ni	38	58—1.95, 60—5.61, 61—91.38, 62—1.07
^{62}Ni	11	58—0.47, 60—0.56, 61—0.22, 62—98.75
^{64}Ni	15	58—0.96, 60—0.71, 62—0.40, 64—97.93
^{63}Cu	52	63—99.9, 65—0.10
^{65}Cu	56	63—0.30, 65—99.70
^{64}Zn	60	64—97.87, 66—1.18, 67—0.21, 68—0.74
^{66}Zn	47	64—0.82, 66—98.84, 67—0.11, 68—0.22
^{68}Zn	60	64—0.38, 66—0.34, 67—0.22, 68—98.97, 70—0.08
^{70}Zn	4	62—8.53, 66—5.46, 67—1.10, 68—6.97, 70—77.94

of ~2 keV. This pattern appears in the Ge(Li) detector spectrum as a broadened peak. Since the hf structure can be readily calculated[24] if the magnetic dipole and electric quadrupole nuclear moments are known, the effect is corrected by fitting the data with a fixed multiplet of lines rather than a single line. The calculation of the hf structure was made using the data given in Ref. 25. Because the hf splitting was not resolved by our detector, it had only a minor effect on the observed line centroids since static hf splitting does not alter the "center of gravity" of the line. In the present measurements the difference in the centroid obtained by fitting a single Gaussian as compared with the appropriate hf structure pattern was typically 30 eV.

To extract precise energy values from the x-ray spectra it is necessary that the functional form which is fitted to the data accurately represent the response function of the Ge(Li) detector. Ideally the response of the detector to a monoenergetic line would be a pure Gaussian. In a real spectrometer system there is some departure from the ideal caused by incomplete charge collection in the detector and by imperfections in the pole-zero compensation and the base-line restoration of the amplifier. Trials with several different line-shape representations indicated that the following function gave a satisfactory representation of the observed line shape:

$$y = N \exp\left(-\frac{(x-x_0)^2}{2\sigma^2}\right) + \alpha N \exp\left(\frac{\beta}{\sigma}(x-x_0)\right), \quad \text{for } x \leq x_0;$$

$$y = N(1+\alpha)\exp\left(-\frac{(x-x_0)^2}{2\sigma^2}\right), \quad \text{for } x > x_0.$$

This function is an approximate representation of a δ function, with a low-energy exponentially decreasing tail, convoluted with a Gaussian. The tail parameters, determined from fits to calibration lines which were stored simultaneously with the x-ray data and held fixed in fitting the x-ray lines, were typically $\alpha = 0.35$ and $\beta = 0.75$. In addition to the usual χ^2 criterion for judging the adequacy of the line-shape representation, we have in these measurements an additional, and perhaps more sensitive, criterion, namely, the accuracy with which the theoretically predictable fine-structure splitting is reproduced. Our results regarding this point are discussed in Sec. V B.

The least-squares data fitting procedure results (after appropriate correction for isotopic impurities and hf structure) in line centroid values for the $K\alpha_1$ and $K\alpha_2$ x-ray transitions. These centroids were converted into energy values using the simultaneously stored calibration lines. In making this conversion two effects must be considered: (1) nonlinearity of the Ge(Li) detector and associated electronic systems; (2) geometrical effects introduced by the different positions of the calibration sources and targets with respect to the Ge(Li) detector.

The magnitude of the first effect was evaluated by making a series of measurements, interspersed with the data runs, of the calibration sources listed in Table II. Together, these sources produced a sequence of 10 precisely known reference points within the energy range of interest (1.0–1.7 MeV), from which nonlinearity was judged. These measurements consistently indicated a linear relationship between fitted line centroid and energy to well within the accuracy of the reference lines (~30 eV). This conclusion was also supported by measurements made on the system with a precision (20 ppm) computer-controlled pulse generator and by other γ-ray measurements which permitted nonlinearity to be evaluated independently of standard reference energies.[26] Although no adjustment of the linearly computed energy values has been made to correct nonlinear effects, an uncertainty of 20 eV has been included in the computation of the estimated errors in these values (see Sec. V B). The geometrical effect, which is primarily a function of the direction of photon incidence with respect to the direction of the electric field vector in the detector, is expected to be small in a true-coaxial detector because of the detector symmetry. Indeed, energy measurements made by comparing sources placed in various positions within a $\pm 40^\circ$ cone around the detector axis indicated no detectable (< 10 eV) angular dependence in the 1.5-MeV energy region. The geometrical effect has therefore been ignored in analyzing the data, although the precaution was taken during the runs of permuting the various targets among the three possible target positions.

A. Isotope and isotone shifts

As has been mentioned, the spectra from three nuclei were collected simultaneously to reduce the influence of various possible instabilities (e.g., electronic gain shifts) on the isotope and isotone shift values. In addition, each isotope was measured several times, each time with various combinations of other nearby nuclides. In total, 27 runs, each with 3 targets, were made with 16 isotopes.

To obtain "best values" for the shifts among the 16 isotopes, a weighted least-squares adjustment was made. In this adjustment the variables were

the 15 energy differences between each isotope and the (arbitrarily chosen) lowest energy isotope ^{58}Fe. The input data for the adjustment were the 54 ($=2\times27$) shift values derived from the 27 runs. (Note that a third shift value is available from each run, but it is numerically equal to the sum of the other two shift values and thus contains no additional information.) The weighting for the least-squares adjustment was done according to the statistical accuracy of the data values. The analysis is complicated here by the fact that the two shift values derived from each run are not statistically independent since they involve a common measurement. This complication is treated in the least-squares procedure by using a two-dimensional weight matrix (cf. Ref. 27). The procedure was performed separately for the $2p_{3/2}$-$1s_{1/2}$ and $2p_{1/2}$-$1s_{1/2}$ shifts; the values of χ^2 per degree of freedom for the two adjustments were 1.1 and 1.2, respectively. The low χ^2 values indicate that the shift values from all 27 runs are quite consistent.

To present our results in the most generally useful form we have elected to combine the $K\alpha_1$ and $K\alpha_2$ shift values into a single array by using the theoretically calculated fine-structure (FS) splitting of each isotope.[28] The results, expressed in terms of the $2p_{3/2}$-$1s_{1/2}$ shifts, are given in Table IV. The uncertainty in each experimental value, calculated by including both diagonal and off-diagonal elements of the error matrix, is also listed. In fact, it is necessary to present the shift values in the form of a matrix only so that the correlated errors can be properly listed. It should be mentioned that all error values quoted here (Table IV and V) have been multiplied by $\sqrt{\chi^2}$ to include certain types of possible systematic errors.

B. Absolute transition energies

In addition to the shift values, our data also provide values of the absolute $K\alpha_1$ and $K\alpha_2$ transition energies (Table V). These values were derived using the following procedure. A second least-squares adjustment was performed in which only a single parameter, the transition energy of ^{58}Fe, was allowed to vary, while the transition energy *differences* between ^{58}Fe and the other 15 nuclei were held fixed at the values which resulted from the first (shift) adjustment. The input data for the second adjustment were the 81 ($=3\times27$) measured transition-energy values. The result is a set of least-squares-adjusted transition energies which are constrained to be consistent with the shift values. The χ^2 per degree of freedom for the $K\alpha_1$ and $K\alpha_2$ fits were 1.9 and 1.3, respectively. These low values again indicate that no serious systematic error exists in the data, even when considered as absolute measurements. In fact, the low χ^2 values suggest that the numerical results would not have been greatly different if only a simple averaging technique had been used to derive the shift values.

It should be noted that the theoretical FS splitting has not been imposed upon the absolute transition-energy values listed in Table V, since the $K\alpha_1$ and $K\alpha_2$ values have been analyzed independently. The results are, however, reasonably consistent with the theoretical FS splittings. The only significant deviation occurs in the case of ^{59}Co, where we obtain an FS splitting slightly higher than the theoretical value. The uncertainties attached to the transition energies have been derived by quadratic addition of terms arising from several sources of possible error: (1) the statistical error in the location of the line centroids; (2) a fitting uncertainty (20 and 40 eV for the $K\alpha_1$ and $K\alpha_2$ lines, respectively) which results from the fact the the $K\alpha$ lines are not completely resolved (this term was estimated by comparing the observed FS splitting with the theoretical values); (3) the uncertainty (~30 eV) of the literature values of the calibration energies; and (4) an upper limit on possible electronic and detector system nonlinearity (20 eV).

Since the $K\alpha_1$ and $K\alpha_2$ transitions contain essentially equivalent information about the nuclear charge distribution, it is convenient to combine these two measured values into a single number which can then be used to deduce the charge parameter R_k. Such a combined value, derived by making a weighted combination of the measured $K\alpha_1$ and $K\alpha_2$ values using the theoretical FS splitting, is given in the third column of Table V. The combined value is expressed, like the shift values of Table IV, in terms of the $K\alpha_1$ transition energy.

The present results for transition energies and for isotope shifts are compared with the limited number of previous measurements of these quantities in Table VI. In general the agreement seems to be satisfactory. The only exceptions are perhaps the $^{60\text{-}62}$Ni and $^{63\text{-}65}$Cu values of Ehrlich,[23] for which, in the former case, we find a considerably larger, and in the latter case, a substantially smaller isotope shift than he reported.

VI. CHARGE RADII

Following the procedure discussed in Sec. II, values of the Barrett radius were derived from the data by using a two-parameter Fermi representation of the nuclear charge distribution:

$$\rho=\rho_0[1+e^{(r-c)/a}]^{-1}.$$

TABLE IV. Least-squares adusted isotope and isotone shift values, expressed in terms of the $2p_{3/2}$-$1s_{1/2}$ transition energy (keV). The experimental uncertainty in eV is listed in italics under each value. Corrections have been applied for hyperfine splitting and isotopic impurities (see text). The values directly measured are in italics; all others are derived from the least-squares adjustment.

	^{58}Fe	^{57}Fe	^{56}Fe	^{54}Fe	^{59}Co	^{64}Ni	^{62}Ni	^{61}Ni	^{60}Ni	^{58}Ni	^{65}Cu	^{63}Cu	^{70}Zn	^{68}Zn	^{66}Zn
^{57}Fe	1.436														
	50														
^{56}Fe	*2.569*	*1.133*													
	33	*38*													
^{54}Fe	*5.526*	4.090	*2.957*												
	38	*49*	*31*												
^{59}Co	86.976	*85.540*	*84.407*	81.450											
	49	*44*	*36*	*48*											
^{64}Ni	170.745	169.309	168.175	165.218	83.769										
	61	*57*	*50*	*59*	*47*										
^{62}Ni	172.345	170.908	169.775	166.818	85.368	*1.600*									
	56	*52*	*45*	*55*	*41*	*29*									
^{61}Ni	173.909	172.473	171.339	168.382	*86.933*	3.164	*1.564*								
	61	*57*	*51*	*60*	*45*	*46*	*41*								
^{60}Ni	174.884	173.448	*172.315*	169.358	*87.908*	*4.140*	*2.540*	*0.976*							
	52	*48*	*40*	*51*	*35*	*33*	*26*	*36*							
^{58}Ni	178.079	*176.643*	*175.510*	172.553	*91.103*	7.334	*5.734*	4.170	*3.195*						
	47	*42*	*33*	*45*	*34*	*43*	*36*	*45*	*31*						
^{65}Cu	258.031	256.595	255.462	252.505	171.055	*87.286*	*85.686*	84.122	83.147	*79.952*					
	62	*58*	*51*	*60*	*48*	*33*	*31*	*48*	*35*	*44*					
^{63}Cu	259.949	258.512	257.379	254.422	172.972	89.204	*87.604*	86.040	*85.064*	81.870	*1.918*				
	61	*57*	*50*	*59*	*47*	*37*	*29*	*47*	*33*	*43*	*34*				
^{70}Zn	342.413	340.977	339.844	336.887	255.437	171.668	170.068	168.504	*167.529*	164.334	*84.382*	82.464			
	121	*119*	*116*	*120*	*114*	*112*	*110*	*115*	*109*	*113*	*111*	*112*			
^{68}Zn	344.278	342.842	341.709	338.752	257.302	173.533	171.934	170.369	*169.394*	166.199	86.247	84.330	*1.865*		
	62	*58*	*51*	*61*	*49*	*38*	*33*	*49*	*35*	*44*	*38*	*36*	*111*		
^{66}Zn	346.059	344.623	343.490	340.533	259.083	*175.315*	*173.715*	172.151	171.175	167.980	*88.028*	86.111	*3.646*	*1.781*	
	61	*58*	*50*	*60*	*47*	*32*	*30*	*47*	*33*	*43*	*33*	*34*	*111*	*26*	
^{64}Zn	348.234	346.797	345.664	342.707	261.257	177.489	*175.889*	174.325	173.349	170.155	*90.203*	*88.285*	5.821	*3.955*	*2.174*
	61	*57*	*51*	*60*	*48*	*36*	*30*	*47*	*34*	*44*	*35*	*31*	*111*	*27*	*27*

TABLE V. Measured $2p_{1/2}$-$1s_{1/2}$ and $2p_{3/2}$-$1s_{1/2}$ muonic x-ray energies.

Isotope	Transition energy (keV) $2p_{1/2}$-$1s_{1/2}$	$2p_{3/2}$-$1s_{1/2}$	Combined value [a]
^{54}Fe	1255.849(63)	1260.011(48)	1260.011(45)
^{56}Fe	1252.919(58)	1257.047(44)	1257.054(42)
^{57}Fe	1251.823(73)	1255.896(56)	1255.921(51)
^{58}Fe	1250.381(67)	1254.460(54)	1254.485(49)
^{59}Co	1336.553(65)	1341.500(50)	1341.461(46)
^{58}Ni	1427.112(60)	1432.534(46)	1432.564(44)
^{60}Ni	1423.860(58)	1429.360(45)	1429.369(43)
^{61}Ni	1422.849(69)	1428.397(54)	1428.393(49)
^{62}Ni	1421.342(59)	1426.814(45)	1426.829(43)
^{64}Ni	1419.708(63)	1425.226(49)	1425.229(46)
^{63}Cu	1508.052(60)	1514.452(47)	1514.433(44)
^{65}Cu	1506.147(62)	1512.534(49)	1512.516(45)
^{64}Zn	1595.528(59)	1602.709(47)	1602.718(44)
^{66}Zn	1593.313(61)	1600.553(45)	1600.544(43)
^{68}Zn	1591.573(60)	1598.760(46)	1598.763(44)
^{70}Zn	1589.863(180)	1596.817(131)	1596.898(109)

[a] Expressed in terms of a $K\alpha_1$ transition energy (see Sec. V B).

A fit to the observed $2p_{3/2}$-$1s_{1/2}$ muonic transition energy was made, varying only the half-density radius c. The skin thickness parameter a was fixed at 0.55 fm. The equivalent radii R_k were then determined using the values α and k listed by Engfer *et al.*[1] for each isotope. The values of α and k were deduced in Ref. 1 using the following procedure. First, the parameter α was determined from a fit to the difference of the potential generated from the bound muon, $V_\mu^i(r) - V_\mu^f(r)$, for the $2p_{1/2}$-$1s_{1/2}$ transition. It was observed that α varies linearly with Z and can be approximated by

TABLE VI. Comparison with previous measurements.

Isotope(s)	Measured quantity	Present value (keV)	Previous measurements (keV)
^{56}Fe	$K\alpha_1$ energy	1257.047(44)	1257.150(60) [a]
^{59}Co	$K\alpha_1$ energy	1341.500(50)	1343.4(5.0) [b,c]
^{60}Ni	$K\alpha_1$ energy	1429.360(45)	1429.4(0.6) [b,d]
^{63}Cu	$K\alpha_1$ energy	1514.452(47)	1513.1(0.6) [b,d]
^{66}Zn	$K\alpha_1$ energy	1600.553(45)	1600.15(0.40) [e]
^{68}Zn	$K\alpha_1$ energy	1598.760(46)	1598.22(0.39) [e]
$^{54-56}$Fe	Isotope shift	2.956(32)	2.970(120) [d]
$^{56-57}$Fe	Isotope shift	1.137(38)	1.250(200) [d]
$^{58-60}$Ni	Isotope shift	3.196(32)	3.140(140) [d]
$^{60-61}$Ni	Isotope shift	0.977(37)	0.970(180) [d]
$^{60-62}$Ni	Isotope shift	2.539(26)	2.000(170) [d]
$^{63-65}$Cu	Isotope shift	1.916(35)	2.310(160) [d], 2.130(80) [f]
$^{66-68}$Zn	Isotope shift	1.782(26)	1.930(360) [g]

[a] T. Böhringer, Travail de Diplôme, ETH Zürich, 1971 (unpublished).
[b] The listed value has been converted from a $2p$-$1s$ center-of gravity measurement to an equivalent $2p_{3/2}$-$1s_{1/2}$ value by adding $\frac{1}{3}$ of the theoretical FS splitting.
[c] D. Quitmann *et al.*, Nucl. Phys. 51, 609 (1964).
[d] R. D. Ehrlich, Phys. Rev. 173, 1088 (1968).
[e] D. A. Jenkins *et al.*, Phys. Lett. 32B, 267 (1970).
[f] E. R. Macagno *et al.*, Phys. Rev. C 1, 1202 (1970).
[g] D. A. Jenkins *et al.*, Phys. Rev. C 2, 458 (1970).

the formula

$$\alpha = 0.03661 + (1.4194 \times 10^{-3})Z.$$

With the value of α thus determined, the parameters A, B, and k of Eq. (2) were fitted using a two-parameter Fermi charge distribution with $t = 4a \ln 3$ fixed at 2.3 fm. The fit of Ref. 1 was done with a weighting function of $r^4\rho(r)$ which emphasizes the nuclear surface region where the charge distribution differences are largest.

Table VII lists for our data the values of α and k and the equivalent radii R_k calculated using Eq. (3). The errors in R_k are derived by multiplying the experimental error by $C_Z = -dR_k/dE$. The error in these radii due to uncertainties in the higher-order corrections has been discussed in Sec. III.

To verify that the quoted R_k are independent of the charge model, the analysis was also performed using Hartree-Fock charge distributions in which the radial scale factor was adjusted to fit the experimental energies. The resulting equivalent radii were the same as those obtained with the two-parameter charge distribution to within approximately 0.2 *mfm* (10 eV).

The isotope and isotone shifts δR_k listed in Table VIII were calculated by taking the difference of the appropriate R_k values. The errors of the δR_k were computed from the experimental errors of the energy differences (Table IV) by using the sensitivity factors given in column 9 of Table VII. The problem of comparing slightly different parameters of the charge distribution, which arises in the case of the isotone shifts, was investigated by using a common α and k for all nuclei. With $\alpha = 0.076$ fm^{-1} and $k = 2.123$ (the values given by Engfer[1] for ^{60}Ni), the isotope differences were found to be the same within 0.1 mfm. The δR_k for the isotones increased 0.5 mfm for isotones differing by one proton and 1 mfm for isotones differing by two protons. Since these changes are only of the order of the experimental error, we have chosen to list the "model-independent" values of δR_k.

It is not unusual for the results of theoretical calculations of the nuclear charge distribution to be quoted in terms of an rms charge radius. For this reason we also list in Table VII values of $\langle r^2 \rangle^{1/2}$, using a two-parameter Fermi distribution. It should be kept in mind, however, that such values are not independent of the charge model used.

VII. INTERPRETATION AND CONCLUSIONS

The aim of this experiment has been the systematic study of isotope and isotone shifts in the region near the $Z = 28$ closed shell. A graphical summary of the results is shown in Figs. 5 and 7. In these two figures the shifts between even-A nuclei are shown separately from the odd-even shifts since the physical interpretation is different in these two cases.

TABLE VII. Experimental equivalent radii, interpreted from the "combined" $2p_{3/2} \rightarrow 1s_{1/2}$ transition energies. Fits were made using two-parameter Fermi function charge distributions, with C as given and a fixed at 0.55 fm. Estimated errors in the equivalent radii R_k do not include theoretical uncertainties.

Isotope	Experimental energy (keV)	Nuclear polarization corrections [a] (keV)	All other corrections [a] (keV)	C (fm)	$\langle r^2 \rangle^{1/2}$ (fm)	α	k	C_Z (mfm/keV)	R_k (fm)
^{54}Fe	1260.011(45)	0.546	9.768	3.98097	3.700	0.074	2.121	−18.1	4.7387(8)
^{56}Fe	1257.054(42)	0.582	9.718	4.04735	3.743	0.074	2.121	−18.1	4.7941(8)
^{57}Fe	1255.921(51)	0.600	9.701	4.07296	3.759	0.074	2.121	−18.1	4.8155(9)
^{58}Fe	1254.485(49)	0.624	9.678	4.10513	3.780	0.074	2.121	−18.1	4.8425(9)
^{59}Co	1341.461(46)	0.588	10.382	4.12450	3.793	0.075	2.121	−16.2	4.8581(7)
^{58}Ni	1432.564(44)	0.689	11.134	4.10687	3.781	0.076	2.123	−14.5	4.8428(6)
^{60}Ni	1429.369(43)	0.693	11.083	4.16295	3.818	0.076	2.123	−14.5	4.8900(6)
^{61}Ni	1428.393(49)	0.632	11.068	4.17918	3.829	0.076	2.123	−14.5	4.9037(7)
^{62}Ni	1426.829(43)	0.703	11.042	4.20767	3.847	0.076	2.123	−14.5	4.9278(6)
^{64}Ni	1425.229(46)	0.725	11.015	4.23639	3.866	0.076	2.123	−14.5	4.9521(7)
^{63}Cu	1514.433(44)	0.739	11.724	4.26910	3.888	0.078	2.127	−13.1	4.9789(6)
^{65}Cu	1512.516(45)	0.749	11.693	4.29959	3.908	0.078	2.127	−13.1	5.0048(7)
^{64}Zn	1602.718(44)	0.857	12.401	4.33742	3.933	0.079	2.130	−11.9	5.0366(5)
^{66}Zn	1600.544(43)	0.909	12.367	4.36910	3.954	0.079	2.130	−11.9	5.0637(5)
^{68}Zn	1598.763(44)	0.917	12.337	4.39462	3.971	0.079	2.130	−11.9	5.0855(5)
^{70}Zn	1596.898(109)	0.973	12.306	4.42190	3.989	0.079	2.130	−11.9	5.1088(13)

[a] Itemized in Table I for selected nuclei.

TABLE VIII. Differences in experimental equivalent radii for $\Delta A = 1, 2$. The experimental error is listed in parentheses following each value. Errors due to theoretical uncertainties are discussed in Secs. III and VI.

Isotopes	δR_k (mfm)	Isotopes	δR_k (mfm)
$\Delta n = 1$		$\Delta n = 2$	
^{57}Fe-^{56}Fe	21.4 (0.7)	^{56}Fe-^{54}Fe	55.4 (0.6)
^{58}Fe-^{57}Fe	27.0 (0.9)	^{58}Fe-^{56}Fe	48.4 (0.6)
^{61}Ni-^{60}Ni	13.7 (0.5)	^{60}Ni-^{58}Ni	47.2 (0.4)
^{62}Ni-^{61}Ni	24.1 (0.6)	^{62}Ni-^{60}Ni	37.8 (0.4)
		^{64}Ni-^{62}Ni	24.3 (0.4)
		^{65}Cu-^{63}Cu	25.9 (0.4)
		^{66}Zn-^{64}Zn	27.1 (0.3)
		^{68}Zn-^{66}Zn	21.8 (0.3)
		^{70}Zn-^{68}Zn	23.3 (1.3)
$\Delta p = 1$		$\Delta p = 2$	
^{59}Co-^{58}Fe	15.6 (0.8)	^{58}Ni-^{56}Fe	48.7 (0.5)
^{60}Ni-^{59}Co	31.9 (0.5)	^{60}Ni-^{58}Fe	47.5 (0.8)
^{63}Cu-^{62}Ni	51.1 (0.4)	^{64}Zn-^{62}Ni	108.8 (0.4)
^{64}Zn-^{63}Cu	57.7 (0.4)	^{66}Zn-^{64}Ni	111.6 (0.4)
^{65}Cu-^{64}Ni	52.7 (0.5)		
^{66}Zn-^{65}Cu	58.9 (0.4)		

A. Shifts between even nuclei

An examination of the even-isotone shifts suggests a strong shell effect. Namely, the addition of the two protons which complete the $1f_{7/2}$ proton shell (^{56}Fe → ^{58}Ni or ^{58}Fe → ^{60}Ni) causes an increase in radius of $\delta R_k = 48 \pm 1$ mfm. In contrast, the addition of two more protons, i.e., the first two protons in the $2p_{3/2}$ shell (^{62}Ni → ^{64}Zn or ^{64}Ni → ^{66}Zn), causes an increase of approximately 110 mfm. In the latter case the increase is more than twice as large as in the former. This is qualitatively understood within the framework of the shell model simply by the fact that the $2p_{3/2}$ shell has a greater radius than the $1f_{7/2}$ shell. Note that the effect seems to be quite independent of the number of neutrons.

As protons are added to a particular orbital one would expect the successive increases in nuclear radius to get progressively smaller, since particles with the same radial charge distribution are being added (indeed, if protons could be added indefinitely in the same orbital, the nuclear charge radius would only asymptotically approach a charge radius corresponding to that particular orbital). When an orbital is filled and additional protons must enter a higher shell, one would expect a sudden increase in the isotone shift. This primitive model, of course, ignores the fact that nucleons do not occupy pure shell-model states and that changes in core deformation can occur with increasing A. However, our data seem to confirm the periodic fluctuation of isotone shifts around an $A^{1/3}$ law average, which the shell model implies.

The isotope-shift data, which cover the region between the beginning at the $2p_{3/2}$ neutron shell at $N = 28$ and the closure of the $2p_{1/2}$ neutron shell

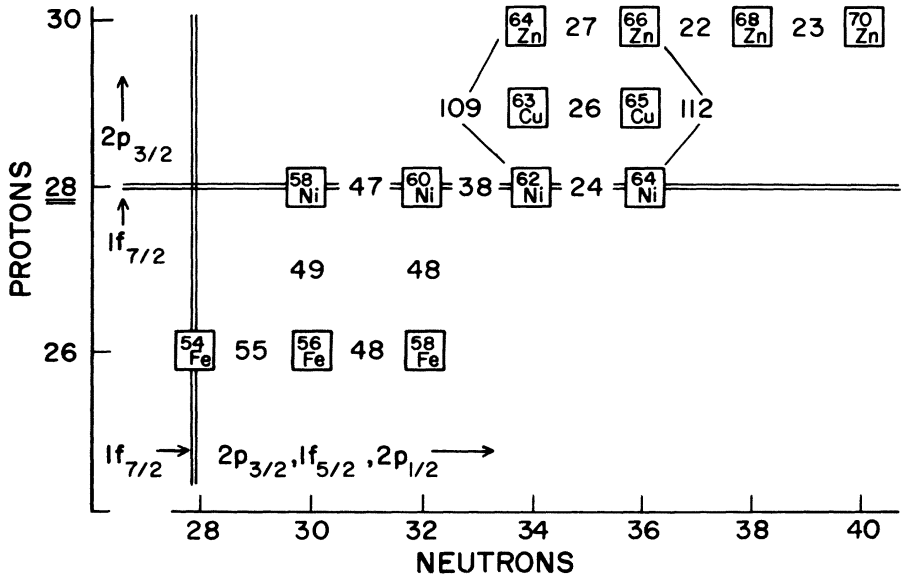

FIG. 5. Differences in the Barrett equivalent radii for adjacent even-even nuclei (mfm). The experimental uncertainties in these values are typically 0.7 mfm (see Table VIII).

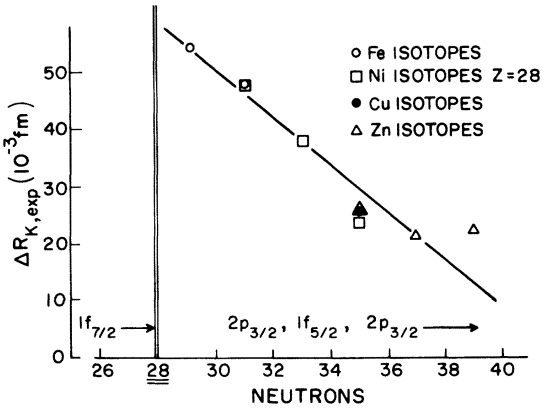

FIG. 6. Isotope shifts for $\Delta N = 2$ as determined in this work. The experimental uncertainties are smaller than the plotted points.

at $N = 40$, are plotted as a function of N in Fig. 6. The most striking feature of the isotope shifts in this region is the uniform decrease with increasing N. Note also that the shift values are *essentially independent of* Z. We find this rather surprising since one might expect that the effect on the charge distribution of the addition of neutrons to the closed-proton shell (and presumably stiffer) Ni isotopes would be considerably less than the effect in Cu or Zn. This independence of the proton configuration suggests that the added neutrons interact with the entire proton core rather than with the valence protons. It is apparent from our data that this interaction decreases in effect as one progresses through a major shell. However, we have no detailed explanation for the approximately linear decrease of the observed isotope shifts.

A realistic description of the charge distribution requires the solution of a many-body problem. A number of many-body theories have so far been constructed, with various degrees of generality and containing various mixtures of phenomenology. One of the most general of these is deformed Hartree-Fock theory. Some results of a deformed Hartree-Fock calculation are discussed in Sec. VII C.

B. Odd-even shifts

When comparing nuclei which differ by $\Delta A = 1$, the effect of an unpaired nucleon becomes evident. It is useful to define an odd-even staggering parameter:

$$\gamma(A+1) = \frac{R_k(A+1) - R_k(A)}{\frac{1}{2}[R_k(A+2) - R_k(A)]}, \tag{6}$$

where A is even. Table IX lists this parameter for the present measurements. Values of the odd-even staggering parameter have been determined for a number of nuclei, primarily by electronic x-ray and optical techniques. The existing data were recently summarized and interpreted by Reehal and Sorensen.[29] These authors suggest that odd-even staggering for *isotopes* is qualitatively explained on the basis that the mean-square deformation associated with the zero-point motion of quadrupole vibrations is greater for even than for odd nuclei. Detailed calculations which use the Tamm-Dancoff approximation are presented in Ref. 29 for several nuclei. In general the computation seems to overestimate the effect. This also applies to the only computed example which we have measured (^{61}Ni) where the calculation gives $\gamma = 0.40$ and we observe 0.72.

TABLE IX. Measured odd-even staggering parameter values.

Isotope sequence	γ
Isotopes	
^{56}Fe-^{57}Fe-^{58}Fe	0.88 (0.03)
^{60}Ni-^{61}Ni-^{62}Ni	0.72 (0.03)
Isotones	
^{58}Fe-^{59}Co-^{60}Ni	0.66 (0.04)
^{62}Ni-^{63}Cu-^{64}Zn	0.94 (0.01)
^{64}Ni-^{65}Cu-^{66}Zn	0.94 (0.01)

In addition to the odd-even staggering for neutrons, we have measured three odd-proton cases. Muonic x-ray measurements are able to give accurate values for isotone odd-even staggering effects. Such is not the case for optical and electronic x-ray methods since the uncertainty intro-

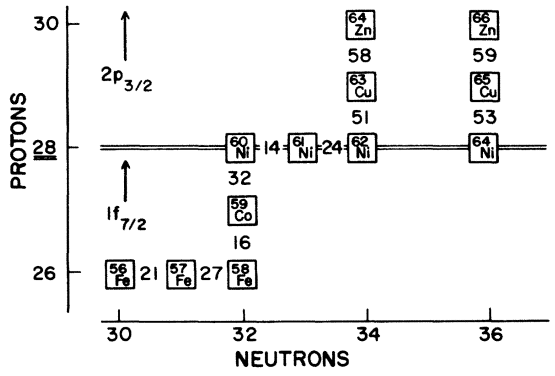

FIG. 7. Differences in the Barrett equivalent radii for adjacent odd-even nuclei (mfm). The experimental uncertainties in these values are typically 0.7 mfm (see Table VIII).

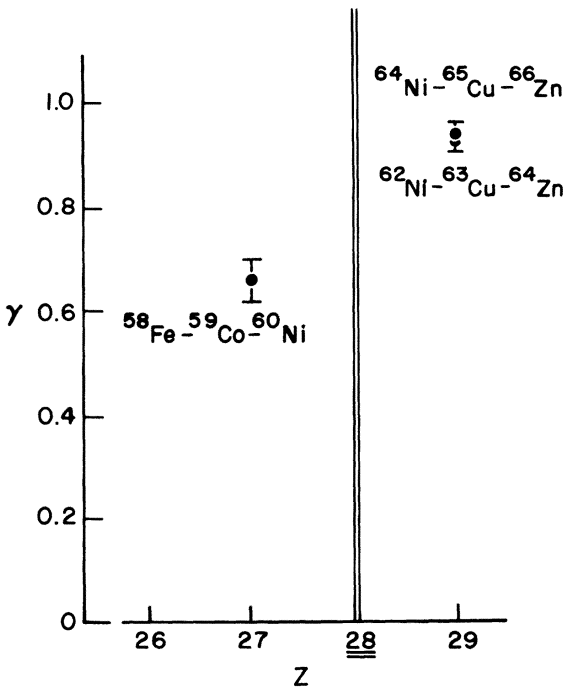

FIG. 8. Values of the odd-even staggering parameter [Eq. (6)] for isotones which bracket the $Z=28$ closed shell.

duced by the differing electronic configurations of different elements overshadows the nuclear charge effects. The present isotone staggering results are displayed in Fig. 8. We observe a large staggering effect for ^{59}Co, which is just below the $Z=28$ closed shell. In contrast we find essentially no staggering effect for both ^{63}Cu and ^{65}Cu which are immediately above the shell closure. Thus a shell effect is suggested. However, with the limited amount of data available there is no other example with which to compare this observation.

C. Comparison with theoretical calculations

The nuclei considered here have been the subjects of a number of theoretical investigations. Of primarily historical interest are several shell-model calculations[30] for the nickel isotopes, which were based on the closed proton and neutron shells at $Z=28$ and $N=28$. The nuclear core was treated either as inert or as capable of undergoing phenomenological vibrations, so that charge radii are not natural predictions of the calculations. In general, the calculations indicate that the nuclear levels are characterized by considerable mixing among the various neutron single-particle states above the (assumed) closed shell at $N=28$. This qualitative feature is supported by the present data. The absence of significant local fluctuations in the isotope shifts above the $N=28$ shell closure suggests that the amplitudes of the spherical single-particle states in the nuclear wave function are smoothly varying functions of neutron number.

More recently, there have been systematic deformed Hartree-Fock calculations of the ground-state properties of most of these nuclei.[31] These calculations are of direct interest here in that they attempt to predict charge radii. Unfortunately, one of the clear results of these calculations is that the Hartree-Fock approximation *per se* is incapable of making such predictions quantitatively for these nuclei. This limitation is due to the fact that the total nuclear binding energy does not have a well-defined minimum as a function of deformation for most of the nuclei in this region. In this situation, nuclear zero-point motion prohibits the accurate specification of ground-state deformation and the Hartree-Fock approximation of the nuclear wave function by a single Slater determinant is of doubtful validity. Barring the use of a substantially different force, the need of which is not indicated by other successes of current Hartree-Fock theory, this inadequacy should be characteristic of any Hartree-Fock-like theory of these nuclei. It appears that an adequate theory must describe the nucleus with a multiconfigurational approach, such as a superposition of different Hartree-Fock states.

An illustration of the Hartree-Fock results is shown in Fig. 9 for ^{58}Ni. The lower curve is the nuclear binding energy as a function of the intrinsic mass quadrupole moment Q_0. The upper curve is the rms charge radius calculated for the same range of quadrupole moments. Over the range $-200\ \text{fm}^2 < Q_0 < 200\ \text{fm}^2$, where the nuclear binding energy changes only slightly, the computed rms radius varies by approximately 0.05 fm. This large variation is of the same magnitude as the

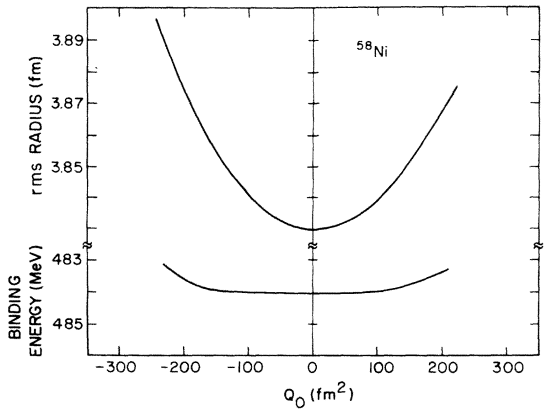

FIG. 9. Binding energy and rms radius of ^{58}Ni as calculated in Ref. 29.

experimentally observed radius differences between neighboring even isotopes. Thus deformed Hartree-Fock theory seems unsuitable for the prediction of charge-radii differences in these nuclei.

The spherically constrained Hartree-Fock calculations,[31] however, predict both the absolute charge radii and the isotope shifts of the Zn and the heavier Ni isotopes rather well. In fact, the calculated radius of ^{70}Zn, the only nucleus considered that has a well-defined minimum of the binding energy at zero deformation, is in nearly perfect agreement with the observed value.

ACKNOWLEDGMENTS

The authors would like to thank A. Bohr, J. Negele, R. Sherr, and A. Zehnder for useful and illuminating discussions concerning this work. Two of us (H.D.W. and G.F.) wish to thank the Deutsche Forschungsgemeinschaft and the Los Alamos Scientific Laboratory for support during their stay in Los Alamos. The support provided for one of us (E.B.S.) by the Deutscher Akademischer Austauschdienst during preparation of the manuscript is gratefully acknowledged.

---

*Work supported by the U. S. Energy Research and Development Administration and the Deutsche Forschungsgemeinschaft.

†Visitor from the U. S. Energy Research and Development Administration.

‡Visitor from Florida State University.

[1]R. Engfer, H. Schneuwly, J. L. Vuilleumier, H. K. Walter, and A. Zehnder, At. Data Nucl. Data Tables 14, 479 (1974).

[2]E. B. Shera, E. T. Ritter, G. A. Rinker, Jr., M. J. Bennett, R. B. Perkins, H. D. Wohlfahrt, G. Fricke, L. K. Wagner, P. Kleinheinz, R. K. Sheline, R. M. Steffen, and J. W. Negele, Phys. Rev. Lett. 34, 535 (1975) contains a preliminary report on the Fe isotope shift results. Experimental values given in the present paper are derived using a somewhat superior method of analysis and supersede the earlier results. The nuclei in this region are also being studied extensively by electron scattering at the University of Mainz (unpublished).

[3]K. W. Ford and J. G. Wills, Phys. Rev. 185, 1429 (1969).

[4]R. C. Barrett, Phys. Lett. 33B, 388 (1970).

[5]E. A. Uehling, Phys. Rev. 48, 55 (1935); R. Serber, *ibid*. 48, 49 (1935).

[6]L. W. Fullerton and G. A. Rinker, Jr., Phys. Rev. A 13, 1283 (1976).

[7]G. Källen and A. Sabry, K. Dan. Vidensk. Selsk Mat. Fys. Medd. 29, No. 17 (1955).

[8]J. Blomquist, Nucl. Phys. B48, 95 (1972); P. Vogel, At. Data Nucl. Data Tables 14, 600 (1974).

[9]G. A. Rinker, Jr., and L. Wilets, Phys. Rev. A12, 748 (1975).

[10]L. Wilets and G. A. Rinker, Jr., Phys. Rev. Lett. 34, 339 (1975).

[11]J. B. Mann and G. A. Rinker, Jr., Phys. Rev. A11, 385 (1975); P. Vogel, *ibid*. A1, 63 (1973).

[12]R. C. Barrett, S. J. Brodsky, G. W. Erickson, and M. H. Goldhaber, Phys. Rev. 166, 1589 (1968).

[13]H. A. Bethe and J. W. Negele, Nucl. Phys. A117, 575 (1968).

[14]J. L. Friar and J. W. Negele, Phys. Lett. 46B, 5 (1973).

[15]G. A. Rinker, Jr. (unpublished).

[16]B. L. Berman and S. C. Fultz, Rev. Mod. Phys. 47, 713 (1975).

[17]J. S. O'Connell, in *Proceedings of the International Conference on Photonuclear Reactions and Applications, Asilomar, 1973,* edited by B. L. Berman (Lawrence Livermore Laboratory, Univ. of California, 1973), Vol. 1, p. 71.

[18]M. Y. Chen, Phys. Rev. C 1, 1167 (1970); H. F. Skardhamar, Nucl. Phys. A151, 154 (1970).

[19]D. Kessler, H. Mes, A. C. Thompson, H. L. Anderson, M. S. Dixit, C. K. Hargrove, and R. J. McKee, Phys. Rev. C 11, 1719 (1975) and references therein.

[20]H. Backe, R. Engfer, U. Jahnke, E. Kankeleit, R. M. Pearce, C. Petitjean, L. Schellenberg, H. Schneuwly, W. U. Schröder, H. K. Walter, and A. Zehnder, Nucl. Phys. A189, 472 (1972).

[21]M. G. Strauss, L. I. Sifter, F. R. Lenkszus, and R. Brenner, IEEE Trans. Nucl. Sci. NS-15, 518 (1968).

[22]L. R. Biswell and R. E. Rajala, Los Alamos Scientific Laboratory Report No. LA-5144, 1973 (unpublished).

[23]R. D. Ehrlich, Phys. Rev. 173, 1088 (1968).

[24]H. Kopferman, *Nuclear Moments* (Academic, New York, 1958).

[25]G. H. Fuller and V. W. Cohen, Nucl. Data A5, 433 (1969).

[26]E. B. Shera, Phys. Rev. C 12, 1003 (1975).

[27]F. A. Graybill, *Introduction to Linear Statistical Models* (McGraw-Hill, New York, 1961).

[28]Theoretical fine structure splitting values used were (in keV): ^{58,57,56,54}Fe: 4.151, 4.154, 4.156, 4.161; ^{59}Co: 4.810; ^{64,62,61,60,58}Ni: 5.529, 5.533, 5.536, 5.538, 5.546; ^{65,63}Cu: 6.327, 6.332; and ^{70,68,66,64}Zn: 7.192, 7.198, 7.203, 7.209, respectively.

[29]B. S. Reehal and R. A. Sorensen, Nucl. Phys. A161, 385 (1971).

[30]N. Auerbach, Phys. Rev. 163, 1203 (1967) and references therein.

[31]G. A. Rinker and J. W. Negele, in Proceedings of the Sixth International Conference on High Energy Physics and Nuclear Structure, Santa Fe, New Mexico, 9–14 June 1975; and (unpublished).

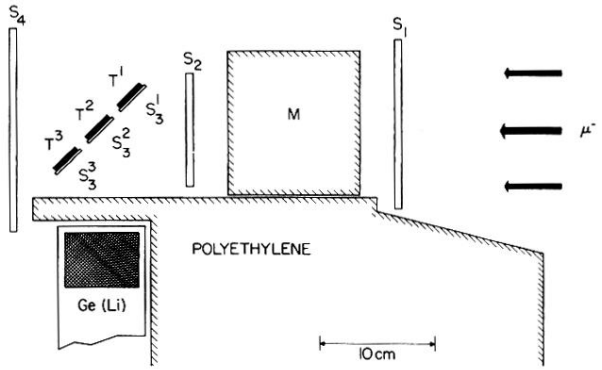

FIG. 3. Arrangement of scintillation counter telescope (S_i), muon moderator (M), targets (T^i), and Ge(Li) detector.